1 Synthesis and Preparation of Oxide Ultrathin Films

Sergio Valeri and Stefania Benedetti

1.1 Introduction

There is a steadily growing interest in the research on oxide surfaces and films, due to their challenging fundamental properties and to their actual and potential applications in catalytic systems, chemical sensors, electronic and magnetic devices, and functional and aesthetic coatings. Special efforts have been directed at the study of ultrathin oxide films [1–11]. Such two-dimensional systems are emerging as important new materials where the relevant phenomena are induced by the extreme vertical confinement, and new phases and structures are stabilized, which cannot be obtained in bulk form. Last but not least, the possible use of thin oxide films as model systems to substitute for bulk oxides has been shown to be very appealing.

Critical properties basically depend on the reduced dimensionality, as well as on the stoichiometry, defectivity, and morphology of the films, on the extent of the crystalline order, and on the sharpness of the interfaces between film and substrate or between different films in multilayers, which are to a great extent determined by the preparation method. Therefore a main driving force in the development of oxide materials in the form of ultrathin films has been the progressive improvement of the fabrication procedures. Since the 1950s, studies of finite size effects in ferroelectrics pointed to a critical film thickness (typically 10 nm) below which ferroelectricity disappears [12]. Improved fabrication techniques have completely changed the picture. Studies on single-crystal, "perfect" ultrathin films have led to the conclusion that perovskite layers down to a very few nanometers in thickness remain ferroelectric [13]. New fabrication methods, alternatives to the conventional thermal oxidation, have enabled the thickness of the gate silicon oxide in metal–oxide–semiconductor field effect transistors (MOSFETs) to decrease to sub-nanometric dimensions, thus reducing both power consumption and power dissipation [14]. The expected, unprecedented properties of ultrathin NiO remained undisclosed until the stabilization of a stoichiometric (1×1)–1 ML NiO/Ag(001) phase with

Oxide Ultrathin Films: Science and Technology, First Edition.
Edited by Gianfranco Pacchioni and Sergio Valeri.
© 2012 WILEY-VCH Verlag GmbH & Co. KGaA, Weinheim.
Published 2012 by WILEY-VCH Verlag GmbH & Co. KGaA

an excellent crystal structure and highly uniform monatomic thickness was achieved, using more aggressive oxidizing species than molecular oxygen in the reactive deposition [15].

Methods for the fabrication of oxide layers include controlled oxidation of bulk metal single crystals and of pre-deposited thin metal films, ion sputtering or laser ablation of bulk oxide targets, and reactive deposition on low-mismatch substrates in a controlled oxidizing atmosphere. In parallel to the physical methods, a number of chemical methods have been exploited, including chemical vapor deposition and liquid-precursor-based techniques, like sol–gel methods and spray deposition. Different methods will not necessarily provide the same results because they imply different nucleation and growth steps. For example, in the case of low-dimensional oxide systems exhibiting a complex phase diagram, the selection of one rather than another approach may be crucial to drive the assembly of the overlayer into a single phase [16]. Comparison between different preparation protocols has been reported in a number of papers [17–22], and two examples are shown in Figures 1.1 and 1.2.

In parallel to the development of preparation protocols, the availability of more and more sophisticated and reliable characterization methods and apparatus was a key factor in pushing both fundamental and technological activities concerning thin and ultrathin oxide films (this aspect is discussed in detail in Chapter 2). In particular a relevant step in analytical capabilities was represented by the use of synchrotron facilities and by the advent of scanning probes. Also, modeling of metal oxide films fully supported the experimental investigations and in a number of cases it provided a major help in resolving film structure and designing more focused experiments [7] (a number of examples are presented in Chapter 4).

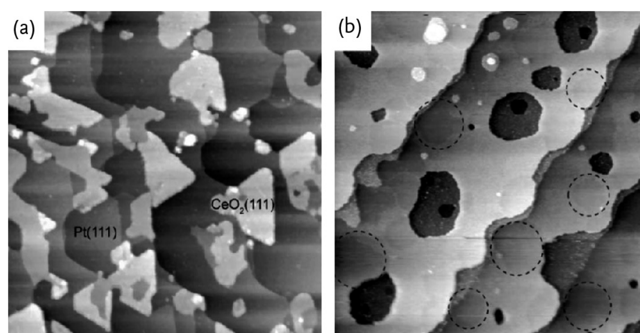

Figure 1.1 Large-area scanning tunneling microscopy (STM) images contrasting two methods for the formation of $CeO_2(111)$ ultrathin films on Pt(111), via surface alloy and reactive deposition. (a) STM image ($200 \times 200\,nm^2$, $V_s = -3.00\,V$, $I_t = 0.10\,nA$) of a 0.5 ML ceria film after oxidation of a Ce/Pt surface alloy at 1000 K in 5×10^{-6} mbar of O_2. (b) STM image ($200 \times 200\,nm^2$, $V_s = -3.20\,V$, $I_t = 0.20\,nA$) of a 0.8 ML ceria film after room temperature reactive deposition of cerium and subsequent annealing at 850 K in 10^{-6} mbar of O_2. Reprinted with permission from [17]. Copyright © 2010 American Chemical Society.

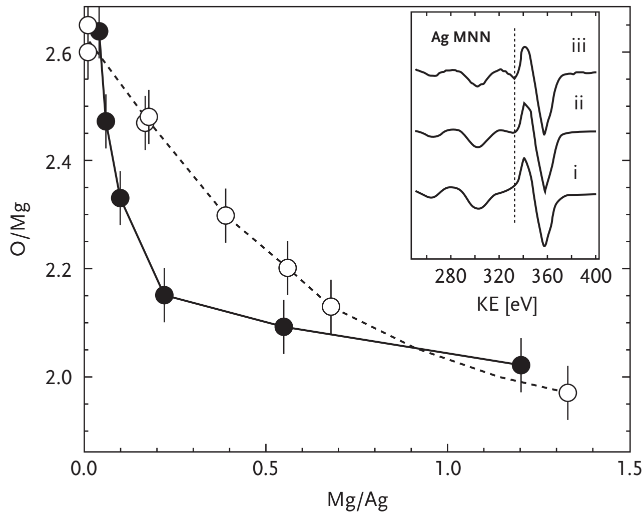

Figure 1.2 O KLL/Mg KLL Auger intensity ratio as a function of the Mg KLL/Ag MNN intensity ratio for both MBE (dashed curve) and sputter deposition (solid curve) of MgO/Ag(001). The inset shows the Ag MNN Auger lineshape for the clean Ag substrate (i) and 6 ML thick sputter-prepared (ii) and MBE (iii) films. Results suggest the occurrence of different growth modes for the MBE and sputter-deposited films, namely the formation of a continuous layer and the formation of islands, respectively. Reprinted with permission from [18]. Copyright © 2001 Elsevier.

1.2
Basic Aspects of Fabrication

A crucial step in fabrication is the establishment of reproducible procedures. An appropriate control of the growth parameters is therefore needed. These are usually the substrate preparation and its temperature during deposition, the growth rate, the nature and partial pressure of the oxidizing agents, the deposition protocol (continuous or stepwise, in the second case eventually alternated with annealing cycles), the temperature and duration of post-deposition heat treatments, and so on.

Ultrathin oxide film fabrication approaches different classes of systems, ranging from "perfect," stoichiometric single-crystal layers or multilayers (model systems), to "row" materials facing the real world, prepared in poor vacuum or in ambient atmosphere by procedures suitable to be transferred to large-scale production. Scalability is a potential of almost all the chemical methods, often at the expense of accurate control of the critical film properties. Examples are methods based on liquid precursors, such as sol–gel methods. In general they lead to films of higher roughness and lower crystal quality, especially when growth rates are high [23]. However, these techniques have proved to be extremely useful to produce a huge number of oxide nanostructures and films, even on complex-shaped objects [24].

In contrast, "perfect" systems are prepared under strictly controlled conditions (usually in ultrahigh vacuum (UHV)) by epitaxy on crystalline substrates. Basic requirements to form epitaxial oxide films of single-crystalline quality are structural similarity and small (a few percent) misfit in lattice constants between the oxide film and the underlying substrate. However, a number of stabilization mechanisms are assumed to be active to allow epitaxial growth even in the presence of relevant mismatch. Substrate oxidation has been proposed to play a determining role for the good epitaxial stabilization of the (111) ceria phase on Pt(111), in spite of the very large lattice mismatch (approximately 40%; P. Luches, personal communication). The growth of stoichiometric MnO(001) monolayer (ML) on a 14.1% mismatched Pd(001) surface can be stabilized by the formation of localized or extended structural defects at the interface [16, 25]. A methodology has been developed to deposit complex oxides on silicon with an alkaline earth oxide buffer layer to allow the epitaxial growth of a wide range of oxides that cannot be grown directly on silicon [26].

Oxide phases (apparently) out-of-equilibrium in terms of either stoichiometry or structural order (strained or defective phases, polar surfaces, etc.) offer the possibility to finely tune specific functionalities. The film strain and its sign largely determine the magnetic anisotropy, the magnitude, and the orientation of magnetic moments close to an interface, as in CoO and NiO antiferromagnetic films prepared on substrates with lattice mismatch of opposite sign, such as MnO(001) and Ag(001) [27, 28]. Ferromagnetic-type behavior observed at low temperatures in thin polycrystalline FeO films (in contrast to the bulk antiferromagnetic properties) has been explained by the defectivity of the films [29]. In ultrathin polar films with a thickness of only a few atomic layers, specific depolarization mechanisms may become effective, therefore motivating the large number of studies of these systems (for recent reviews, see [6, 30]).

The role of the substrate goes far beyond that of a simple passive support and often involves an active participation in the growth process and/or in the film properties. Elastic strain plays a major role in supported, epitaxial oxide nanostructures, where the lattice parameters of the substrate often impose severe constraints on the atomic arrangement in the overlayer, thus affecting structure, morphology, and other properties of epitaxially grown oxide nanolayers [11]. Therefore by the appropriate choice of substrate new classes of systems with tunable physical and chemical properties may be created. As an example, in mixed metal oxide catalysts the oxide substrate has been reported to greatly enhance the catalytic efficiency of the supported ultrathin oxide layer [31]. Preferential sites for the self-organized growth of metallic nanoparticles on oxide films are provided by the periodic displacement of the film surface induced by the misfit dislocation network formed at the overlayer–substrate interface to relieve the mismatch strain (Figure 1.3) [32, 33].

Very reactive substrates such as iron require special care in order to avoid substrate oxidation. For the MgO/Fe system, evaporation of bulk oxide target has been used to pre-deposit a buffer oxide film [34]. In order not to oxidize the Fe_3O_4 substrate to Fe_2O_3 during the preparation of CoO films, growth was initiated by deposition of enough cobalt to be oxidized into 1 ML CoO and subsequent oxygen exposure, thus enabling reactive molecular beam epitaxy (MBE) to be used for the

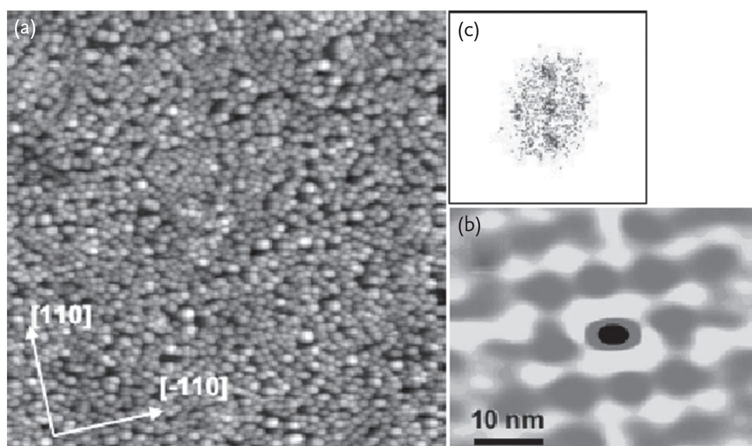

Figure 1.3 (a) Constant current topographic scanning tunneling microscopy (STM) image of 0.15 nm Ni/20 ML CoO/Ag(001). The image size is $200 \times 200\,nm^2$, recorded with $I = 0.2$ nA and $V = 2.2$ V. (b) Two-dimensional self-correlation analysis and (c) Fourier transform of the STM image in (a). Reprinted with permission from [32]. Copyright © 2008 American Physical Society.

subsequent growth of thicker films [35]. Metal surfaces as substrates for oxide nanosystems provide particular attractions not simply because they are easily prepared with atomic-level control but also because they feature a number of technical advantages for microscopic and spectroscopic characterization of physical and chemical properties, for example, avoiding charging problems in scanning tunneling microscopy and electron spectroscopies.

During growth, subtle interplay between kinetic and thermodynamic factors may lead to rather (structurally or chemically) distinct films. In principle, thermodynamics governs the stability conditions; however, kinetic processes can also contribute to the stabilization of ultrathin oxide films, as discussed, for example, for alumina layers on NiAl(110) where the oxygen pressure needed for stability differs greatly from thermodynamic predictions [36]. Recently, the occurrence of strong kinetic effects have been outlined by *in situ* monitoring of dynamic processes at the TiO_x–Pt(111) interface [37]. The kinetic characteristics of the growth process of strontium titanate films on silicon have been used to suppress the oxidation of the substrate surface through the manipulation of two key parameters, namely substrate temperature and oxygen partial pressure, and thereby achieve oxide films with a high degree of crystallinity [38]. Very aggressive oxidizing conditions in terms of high temperature and oxidizing gases also determine the relative importance of kinetics and thermodynamics during film growth.

In order to optimize the growth of stoichiometric films and the sharpness of the oxide–substrate interface, film oxidation should occur at a rate much higher than that of both film growth and substrate oxidation. Under this condition, the growth of understoichiometric (reduced) phases is strongly inhibited. Exposure to molecular oxygen is the standard oxidation procedure, but stronger oxidizing agents

like atomic oxygen, ozone, or gaseous NO_2 can be used, to achieve a higher degree of order and a better control of the stoichiometry and morphology of the oxide–metal interface, as recently demonstrated for a ML of NiO on Ag(001) [15]. The different results in room temperature oxidation of $Pt_3Ti(111)$ surface alloy using either O_2 or NO_2 oxidizing agent were ascribed to the stronger oxidative power of NO_2 gas [19]. Surface structure and termination of oxide films were also reported to strictly depend on the oxygen dosage during growth, as reported for the preparation of hematite [39] and of NiO [40]. A detailed discussion of oxidizing agents and conditions is reported in [2, 11].

In a similar way, for chemical methods the precursor chemistry is of great importance. The low-rate chloride-based SnO_2 atomic layer deposition (ALD) process leads to a film of high surface roughness, a large amount of twin formation, and grain boundaries, as compared to the corresponding iodide-based process. This effect is due to a competing etching process during growth, despite that a lower growth rate is generally assumed to lead to a more surface-controlled growth of higher quality films (Figure 1.4) [41].

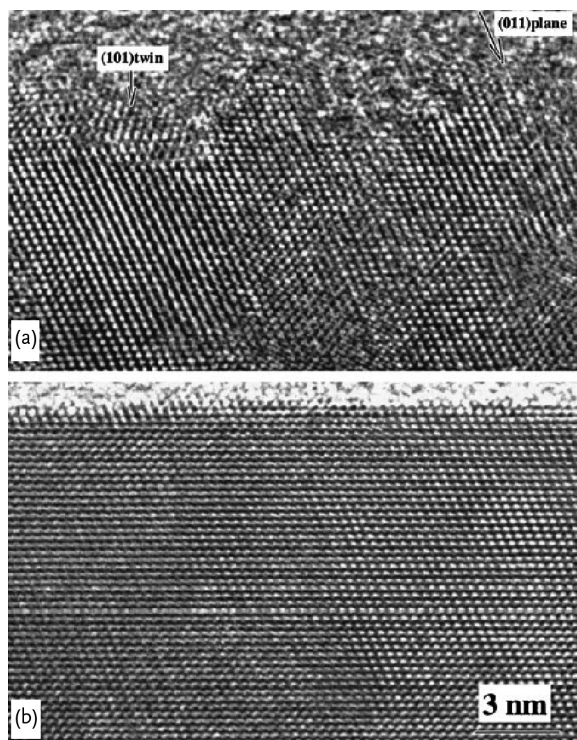

Figure 1.4 High-resolution transmission electron microscopy images of (a) a rough surface of a $SnCl_4$-process SnO_2 film containing a stage facetted with a (011) plane and a (101) twin nucleus and (b) a flat SnO_2 surface of a SnI_4-process film. Reprinted with permission from [41]. Copyright © 2004 Elsevier.

The formation of fully closed films represents an important precondition for a number of applications, for example, with respect to the preparation of regular model catalysts, in order to minimize substrate effects on the surface chemistry. A partially successful approach involved the preparation of ceria films on Ru(0001) [42]. As an alternative system, the growth of CeO_2(111) on Cu(111) has been suggested [43], because of the very small lattice misfit. However, continuous films were obtained only for layer thicknesses of several MLs. A new strategy for the formation of atomically flat ultrathin films has been recently explored, based on growth under kinetically controlled conditions to suppress or reduce diffusion. Deposition at low sample temperature (100 K) in oxygen atmosphere was used, followed by a post-annealing at 770 K, again in oxygen atmosphere [44]. A fully closed film, even in the ML region, has been obtained by this procedure.

1.3 Physical Methods

1.3.1 Controlled Oxidation of Bulk Single-Crystal Surfaces

Ultrathin oxide films can be prepared by directly oxidizing the substrate formed by the parent single crystal. Exposure of metal surfaces to oxygen leads to the moderately rapid formation of a thin oxide layer. At room temperature the oxygen uptake stops once this limit is reached, because the formed oxide passivates the surface, while at higher temperatures the slow growth of a thicker oxide is observed. The simultaneous impingement of argon ions on the substrate during oxygen exposure was used to enhance the oxidation process [45]. However, one of the main drawbacks of this method is that the crystal structures of the films cannot be easily controlled, in spite of the use of highly oriented metal surfaces as substrates. This is particularly expected in specific cases, for example, for the oxidation of magnesium single crystals, since MgO crystallizes in the rocksalt structure and not in the hexagonal close-packed structure of magnesium [46]. Direct oxidation of magnesium single crystals has been observed to result in a rather imperfect oxide film. Beside the true ionic oxide MgO, oxygen in the surface layer has been observed to exist in different states, forming a layer underneath the top layer of the magnesium crystal [46]. Similarly to the MgO case, the direct oxidation of nickel [47, 48], cobalt [49], and iron [20, 50] single crystal surfaces leads to unsatisfactory results. A general finding is that the long-range structural order is poor if the oxide film thickness exceeds 3–5 layers, due to the relatively large mismatch between the single crystals and the majority of their oxides. The composition of TiO_x films prepared by oxidation of single-crystal [51] or polycrystalline [52] substrates greatly depends on the oxygen pressure and substrate temperature during oxidation. Surface oxidation of aluminum single-crystal substrates has been also extensively investigated [53, 54]. The resulting films are not particularly well defined and are often polycrystalline or randomly oriented. However in selected cases, as for

the oxidation of Al(110) at elevated temperatures in oxygen, the formation of a stable stoichiometric Al_2O_3 layer with fairly abrupt interfaces has been observed [55]. A way to make this approach more flexible is to put an oxidizing agent in contact with the surface of an intermetallic alloy crystal where the most reactive metal will preferentially oxidize. This method has been employed to grow AlO_x and TiO_x films [8]. A large quantity of work is related to the NiAl(111) surface of alloy single crystals in low oxygen pressure and at high temperature [36, 56, 57].

1.3.2 Sputtering and Ablation of Oxide Targets

1.3.2.1 Sputter Deposition

In the basic sputtering process, a target is bombarded by energetic ions generated in a direct current- or radio frequency-generated glow discharge plasma situated in front of the target. The bombardment process causes the removal (sputtering) of target atoms or clusters, which may then condense on a substrate as a thin film [58]. The process is limited by low deposition rates and strong substrate heating effects. These limitations have been overcome by the development of magnetron sputtering, where a magnetic field configured parallel to the target surface results in a dense plasma in the target region, giving higher sputtering rates and, therefore, higher deposition rates. Radio frequency magnetron sputtering was used to prepare hematite thin films on stainless steel and Si(001) single-crystal substrates [59], and to deposit ferroelectric $Pb(Zr,Ti)O_3$ on $SrTiO_3/Si$ structures [60]. MgO films were prepared on Ag(001) substrate by Ar^+ ion-beam sputter deposition from a MgO target, and this procedure was reported to favor a larger islanding of the oxide film in the initial deposition stage with respect to other growth procedures [18].

1.3.2.2 Pulsed Laser Deposition

Pulsed laser deposition (PLD) uses a pulsed laser to ablate a target to produce the depositing flux [61, 62]. The laser beam vaporizes the surface of the target and the vapor condenses on a substrate. The laser-induced expulsion produces a plume of material with stoichiometry similar to the target. The kinetic energy of the ablated products is variable from less than one to a few hundred electronvolts. Practical advantages of PLD include the congruent transfer from the target, and the ability to ablate virtually any target. To achieve good-quality thin films, key PLD deposition parameters include deposition temperature, ambient gas pressure, laser energy, and laser pulse repetition rate.

It is generally easier to obtain the desired film stoichiometry for multiple-element materials using PLD than with other deposition technologies; therefore PLD is a reliable method routinely used to prepare epitaxial multicomponent films of complex functional oxides such as cuprates, manganites, and ferroelectric oxides [63–66]. Thin epitaxial $Pb(Zr,Ti)O_3$ films were prepared by PLD on CeO_2/yttria-stabilized zirconia buffered Si(001) substrates [63]. Chemical abruptness and

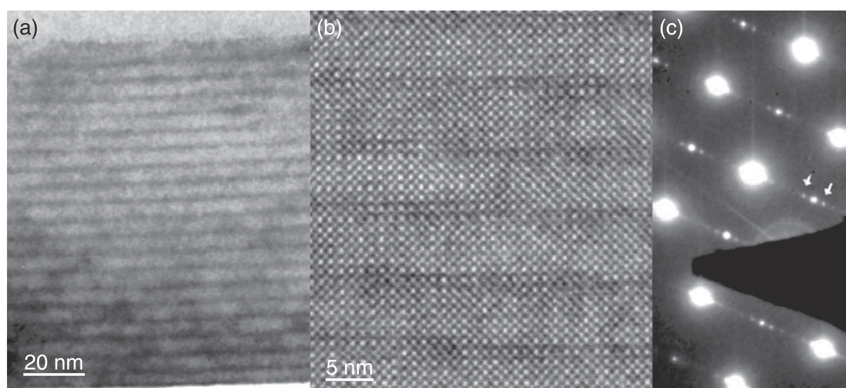

Figure 1.5 Cross-sectional transmission electron microscopy images of a 20-bilayer $PbTiO_3/SrTiO_3$ sample. (a) Bright-field image clearly showing the intended layering of the structure. (b) High-resolution image showing the perfect crystalline structure of the material. (c) Diffraction image demonstrating superlattice periodicity. Reprinted with permission from [65]. Copyright © 2005 American Physical Society.

crystalline perfection of oxide multilayers prepared by PLD now rival those of semiconductor multilayers. It is possible to change from one material to another over a distance of a single unit cell (Figure 1.5) [64, 65]. As a result of improvements in film growth, mobilities of charge carriers have reached values so high that the quantum Hall effect has been achieved at interfaces between oxides, an effect previously limited to interfaces between high-purity semiconductors [66].

UHV PLD also finds applications in the field of single-metal oxides [67–70]. As an example, CeO_2(001) and CeO_2(110) thin films were grown by laser ablation of stoichiometric ceria targets onto single-crystal $SrTiO_3$(001) and $SrTiO_3$(211) substrates, respectively [67]. Evaporation of a solid CeO_2 target has also been achieved by UHV electron beam bombardment to prepare ultrathin (3 nm) ceria layers on Si(111) wafers [71].

1.3.3 Reactive Physical Vapor Deposition

The basic physical vapor deposition (PVD) process requires the source material to be prepared in the gaseous state, to be transported to the substrate, and to be deposited on its surface. Usually the source material is thermally evaporated (e.g., using a Knudsen cell); however, also ion sputtering and laser ablation have been used to prepare source materials in the gaseous state. Most ultrathin oxide films need to be prepared as epitaxial, crystalline layers on a crystalline substrate. Low deposition rates, UHV ambient, and well-controlled partial pressure of the oxidizing agent are the main conditions for this fabrication approach usually referred to as MBE. Reactive MBE occurs with the presence of a gas that reacts with the atoms or molecules of the source material.

1.3.3.1 Film Growth by Sputtering or Ablation of Pure Targets in Oxidizing Atmosphere

NiO thin films have been deposited at room temperature by direct current reactive magnetron sputtering of a nickel target in an Ar^+–O_2 mixed atmosphere on silicon substrates covered with thermally oxidized SiO_2, and a correlation between process parameters and film properties has been established [72]. A similar approach has been used for the growth of CeO_2 layers on Si(100) substrates [73] and for the preparation of tin and indium oxide ultrathin films (basic components of gas-sensitive structures) with thicknesses between 2 and 30 nm on silicon substrates with SiO_2 surface layer [74]. PLD in oxygen atmosphere was used to prepare $SrTiO_3/LaTiO_3$ superlattice films using stoichiometric, crystalline targets [75], and to prepare epitaxial $La_{0.67}Sr_{0.33}MnO_3$ perovskite films on $NdGaO_3$(110) [76].

1.3.3.2 Film Growth by Reactive MBE

Reactive MBE has been widely used to prepare simple metal oxides on a variety of substrates. As an example, MgO has been grown in the form of ultrathin films on Ag(001) [77–80], Fe(001) [81, 82], and Mo(001) [83–86]. Particularly interesting is the use of Mo(001) substrate, because of its high thermal stability and the mismatch of −5.2% with bulk MgO. The mismatch is small enough to allow epitaxial growth, but large enough to emphasize the effect on oxide film structure and morphology. The strain induced in the growing film by the mismatch with the substrate is relieved by the formation of an ordered network of interfacial misfit dislocations. Very thin films show the presence of a regular surface pattern associated with the dislocation network (Figure 1.6a). With increasing thickness, screw dislocations with nonpolar steps appear on the oxide surface (Figure 1.6b) [85, 86].

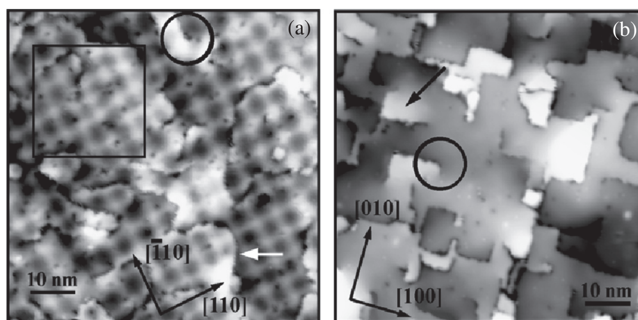

Figure 1.6 Scanning tunneling microscopy images ($70 \times 70\,nm^2$) of MgO films on Mo(001): (a) 2 MLs annealed at 1070 K ($U = 3.5$ V) (white arrow indicates a domain boundary); (b) 15 MLs annealed at 1070 K ($U = 4.8$ V) (black arrow indicates a (110) tilted surface region in proximity of a screw dislocation). Circles indicate examples of screw dislocations. Reprinted with permission from [86]. Copyright © 2008 American Physical Society.

For deposition of MgO on Ag(001), where the lattice mismatch is rather small (−3.2%) compared to the molybdenum case, the appearance of surface tilting parallel to the [100] direction is observed, attributed to the formation of [100] dislocations by the glide system 1/2[110](110) (Figure 1.7) [87, 88]. Similar results have been reported for the MgO/Fe(001) system [82]. In the MgO/Ag(001) system, substrate disruption also occurs, due to the high mobility of silver atoms, with the formation of vacancy islands, embedded MgO islands, and protruding silver and MgO islands, resulting in a complex morphology (Figure 1.8) [80]. The orientation of the islands has been observed along both the [100] [78] and [110] [80] directions. Calculations have proved that [110] polar borders are stabilized by the presence of the metal support, becoming quasi-isoenergetic with respect to the nonpolar borders [89].

In addition to simple metal oxides, also transition metal oxides have been prepared in the form of ultrathin films by reactive MBE. A detailed discussion of the preparation of ferromagnetic NiO, CoO, FeO, α-Fe_2O_3, and MnO thin films is reported in [90]. The occurrence of interfacial dislocation networks has been observed in a number of these oxides, such as NiO/Pd(111) [91], CoO/Ag(001) [32], CoO/Ir(001) [92], FeO/Pt(111) [93], and α-Fe_2O_3/α-Al_2O_3(0001) (Figure 1.9) [94], often resulting in the formation of regular surface patterns of morphological and/or electronic nature.

A number of studies of vanadium oxide films as a function of coverage and thickness explored the entire, complex surface "phase diagram" of this system [95–99]. Several coexisting vanadium oxide phases were often observed, where the oxidation state of the vanadium atoms progressively decreases with increasing

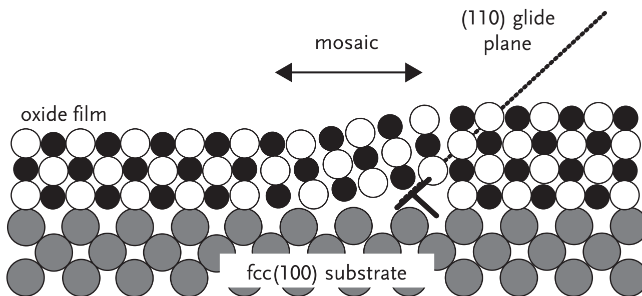

Figure 1.7 Model for the mosaic formation due to interface dislocation with (110) glide plane. Reprinted with permission from [87]. Copyright © 2001 Elsevier.

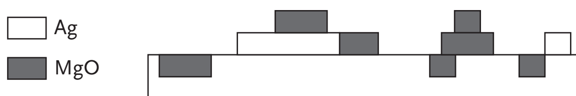

Figure 1.8 Schematic of the morphology of a MgO/Ag(001) interface. Reprinted with permission from [80]. Copyright © 2002 American Physical Society.

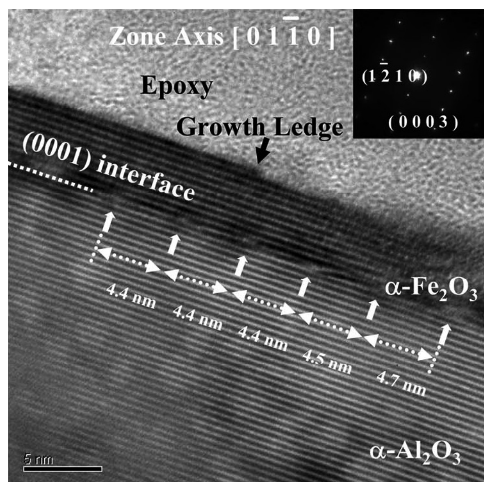

Figure 1.9 High-resolution transmission electron microscopy image of interface misfit dislocations imaged from the (01 1̄0) zone axis. The inset shows the selected area electron diffraction pattern. Reprinted with permission from [94]. Copyright © 2005 American Physical Society.

oxide coverage. Pd(111) [95, 96], Rh(111) [97], and Au(111) [98, 99] surfaces were mainly used as substrates. The reader is referred to recent reviews [7, 11]. Vanadia is also a relevant component of mixed-metal oxides. Vanadia films in the sub-ML to multilayer coverage regime were deposited on the (110) surface of a TiO_2 substrate by reactive MBE, resulting in a mixed-metal oxide system that exhibits a higher catalytic activity and selectivity than the unsupported oxide material. Preparation and catalytic properties of $MO_x/TiO_2(110)$ (M = V, W, Ce) surfaces are discussed in detail in [31].

Similarly to the vanadium oxide case, also titanium oxide films have been prepared by reactive MBE and their surface phase diagram has been investigated in detail. Ultrathin TiO_x films have been grown on various metal surfaces, and a variety of structures and compositions ranging from fully oxidized ($x = 2$) to reduced ones ($1 < x < 2$) have been observed, depending on the coverage and on the oxygen partial pressure during deposition or post-growth annealing. A complex situation with many different phases has been described, for example, for the TiO_x/Pt(111) system [100–103], a particularly interesting system where the growth of TiO_x nanostructures seems to be controlled to a large extent by the interaction with the platinum substrate. Exhaustive reviews have been published [7, 8, 11].

Ultrathin films of CeO_2 were grown on the Pt(111) surface by reactive deposition of cerium using molecular or atomic oxygen as the oxidizing gas. High-temperature treatments in O_2 allowed the fabrication of cerium oxide films with very good quality in terms of morphology and structure. The stoichiometry of the films is mainly CeO_2 and the concentration of Ce^{3+} ions in the film can be reversibly increased by temperature treatments (P. Luches, personal communication).

Reactive MBE has also been used to prepare complex oxide films and nonmetal oxide films. Strontium titanate films were prepared by this method, in direct contact with silicon substrate, with no interfacial silicon dioxide [38]. Synthesis of bilayers of a cuprate metal ($La_{1.65}Sr_{0.45}CuO_4$) and a cuprate insulator (La_2CuO_4) has been carried out using a system equipped with 16 metal sources, where a pure ozone source was used to ensure high oxidizing power. Single-crystal films with atomically smooth surfaces and interfaces were reproducibly fabricated, in which each layer is just three unit cells thick. It has been shown that in these films high-temperature superconductivity occurs within a single CuO_2 plane [104]. Crystalline silica films have been successfully fabricated on a Mo(112) substrate by MBE deposition in an oxygen environment onto an oxygen-precovered surface and subsequent annealing in vacuum. A flat, homogeneous, and well-ordered silica film is formed, which consists of a two-dimensional network of corner-sharing [SiO_4] tetrahedral sites [105, 106].

1.3.4
Post-oxidation of Pre-deposited Thin Metal Films

Oxidation of pre-deposited thin metal films has been explored as a means to reduce the mismatch and improve the quality of the oxide films. However, in general films are not fully oxidized by this procedure and long-range structural order is often not satisfactory. The overall quality of the film is only slightly improved by high-temperature annealing. As an example, by oxygen exposure of magnesium films deposited on Ag (100) only in the topmost few layers is stoichiometric MgO generated, while an amount of nonstoichiometric MgO species are present, which can be reduced but not eliminated by successive annealing processes. The structure of annealed MgO film consists of three domains of (100)-oriented crystallites rotated by 120°, interpreted as being reminiscent of the hexagonal order of the pre-deposited magnesium film [77]. Heteroepitaxial FeO films were first produced by post-oxidation of iron films deposited on Pt(111) and Pt(100) and it was observed that FeO(111) films grew layer-by-layer on both substrates [107]. NiO ultrathin films on Pd(001) were prepared by metal deposition and post-oxidation cycles, and optimization of the growth parameters was discussed. A critical parameter was observed to be the initial dose of nickel evaporated on the clean palladium substrate. It has been demonstrated that post-oxidation is effective in order to obtain epitaxial NiO only if the initial dose of nickel evaporated on the clean Pd(100) substrate exceeds a critical value, corresponding approximately to two equivalent MLs [108]. Vanadium oxide was prepared by post-oxidation of vanadium metal deposited onto a Rh(111) surface at room temperature and subsequent oxidation at 400 °C followed by cooling in oxygen atmosphere [109]. Stabilization of an impurity-free and unreconstructed ML CoO(111) polar film on a metal surface was reported for cobalt ML deposition on a Pt(111) surface and O_2 post-oxidation [110]. A variant of the traditional approach was reported for the growth of a Ti_2O_3 ML on a Pt(100) surface

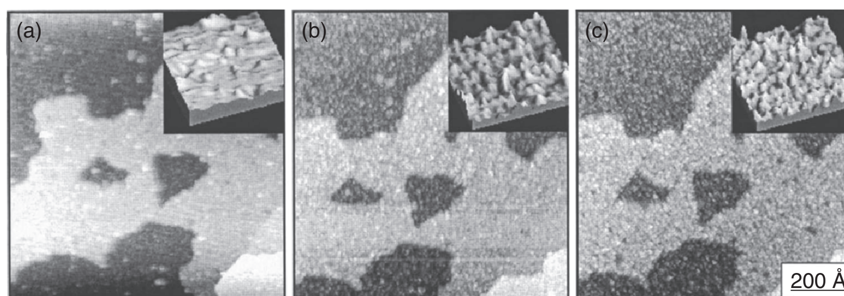

Figure 1.10 Sequence of scanning tunneling microscopy images (1149 × 1148 Å^2) obtained during oxidation of a Ti/Pt(111)-(2 × 2) alloy at 300 K using NO_2 ($V_b = +207$ mV and $I_t = 0.285$ nA). The image in (a) is from the alloy prior to NO_2 exposure. The total NO_2 exposures for (b) and (c) were 34 and 93 L, respectively. The insets are higher resolution images (21 × 22 Å^2) showing r.m.s. roughnesses of (a) 3.5, (b) 5.3, and (c) 7.1 Å. Reprinted with permission from [19]. Copyright © 2008 American Vacuum Society.

[19, 111]. Here, an ordered Pt_3Ti surface alloy was formed prior to the oxidation step with oxygen, nitrogen dioxide, or ozone (Figure 1.10). A similar procedure, but using molecular oxygen, was previously adopted by Knight *et al.* to grow epitaxial manganese oxide by oxidation of a Cu(100)c(2 × 2)-Mn substitutional surface alloy [112].

Metal deposition, post-oxidation, and annealing cycles can be repeated several times to overcome the diffusion limit and obtain stoichiometric oxide films several MLs thick. Epitaxial iron oxide films on Ag(111) were prepared by different procedures [21]. A 10 ML iron deposition followed by oxidation resulted in poorly ordered FeO(111) films but, by the sequential deposition of sub-ML iron films followed by oxidation, a much better crystallographic order has been obtained, up to about 10 Å in thickness.

1.4 Chemical Methods

The use of chemical deposition methods has allowed the large-scale production of thin oxide films on complex-shaped objects at lower cost. The main disadvantage is the reduced control over the deposition and the risk of residues left from the precursors as compared with cleaner PVD methods. These methods can be roughly divided into two main groups, one based on chemical vapor deposition (CVD), the second based on liquid precursors. All these techniques have been extensively used recently for the growth of doped and undoped oxide nanostructured materials with potential applications in areas ranging from electronics, optics, and energy storage to biomedical sciences [113].

1.4.1 Chemical Vapor Deposition

CVD exploits chemical reactions of precursors of the desired material transported by a carrier gas to the substrate, where a set of homogeneous gas-phase reactions and/or heterogeneous chemical reactions take place activated by heaters or by a plasma discharge (plasma-enhanced CVD) [24]. Oxide thin films can be prepared by CVD in various ways. One example is metal-organic chemical vapor deposition (MOCVD), classified according to the use of metal-organics as precursors. MOCVD has been used to grow metal oxide films such as ferroelectric $PbTiO_3$, $PbZrTiO_3$, and $BaTiO_3$ [114] and superconducting copper oxide films [115]. Here substrate, precursor type, and growth temperature are the important factors influencing both the crystal growth direction and the degree of order of the films.

Various simple oxides have been prepared by means of CVD [116]. As an example, MgO on various substrates (Si(001), sapphire, quartz) has been shown to grow in a cubic structure free from undesired phases, with the presence of carbon limited to the outermost layers, because of the oxide reactivity with the outer atmosphere. All the films are characterized by a granular surface morphology, with roughness values always lower than 10 nm. Orientation of the polycrystalline MgO films depends strongly on the precursor and on the substrate temperature [117, 118].

A special modification of CVD is ALD. Here film growth takes place in a cyclic manner by exposure to a first precursor and subsequent exposure to a second precursor [119, 120]. The growth cycles are repeated as many times as required for the desired film thickness. A self-limiting growth mechanism due to the formation of a chemisorbed layer allows accurate thickness control at the atomic level [121, 122]. ALD has been used to deposit oxide materials (such as yttria-stabilized zirconia, doped CeO_x, etc.) for solid oxide fuel cells [123] and for many oxides such as SnO_2 and ZnO used as gas sensors [124–126]. Because of the non-line-of-sight process, this method has been used to prepare coatings of objects with complex shapes. An example is the coating of ZrO_2 nanoparticles with thin homogeneous MgO films a few nanometers thick [127]. ALD is often used to deposit high-k gate oxides in MOSFETs, where the control of ultrathin films is essential. With this method SiO_2 films grow perfectly uniform and flat, substantially indistinguishable from thermally oxidized SiO_2 [14]. Therefore it is possible to control interface roughness and defect densities that can especially affect the mobility of charge carriers. This method has been applied to other high-k dielectric oxides such as Al_2O_3, ZrO_2, and HfO_2 [128]. With the introduction of precursor chemistry and plasma assistance, the need for high substrate temperatures has been reduced, making ALD applicable also for plastic substrates and organic field effect transistors. The example of SnO_2 films grown on α-Al_2O_3 by ALD and CVD using the same precursor combination allows a comparison between the two methods [129]. The ALD process produces films almost perfectly single crystalline and with a low number of defects

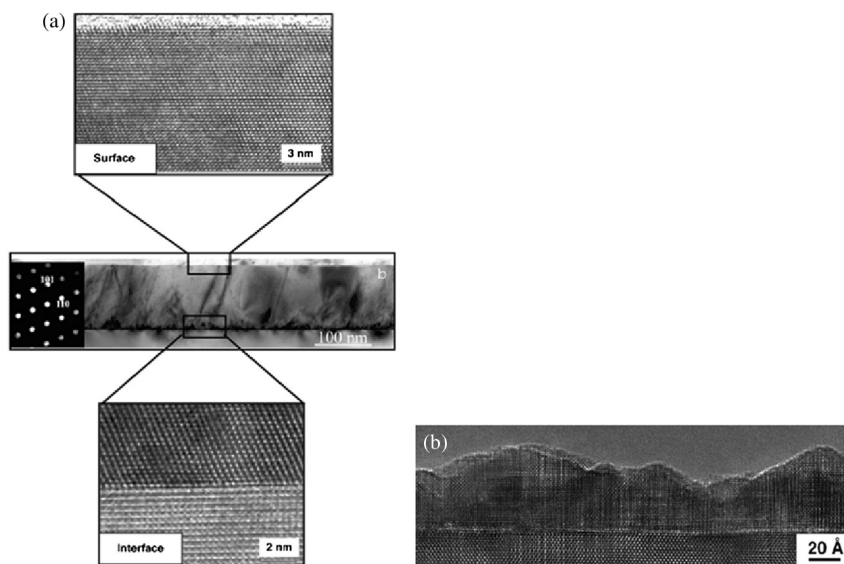

Figure 1.11 Transmission electron microscopy images of a SnO_2 film deposited on α-Al_2O_3(012) substrate (a) by ALD (middle), where high-resolution images of the film surface (top) and film–substrate interface (bottom) are also included and (b) by CVD. Reprinted with permission from [129]. Copyright © 2006 Elsevier.

(Figure 1.11a). Epitaxial films can also be grown at low temperatures by CVD. However, these films contain grain boundaries and have a high surface roughness (Figure 1.11b), in spite of the similar growth rates used.

1.4.2
Liquid-Precursor-Based Thin-Film Deposition Techniques

Wet-chemical processes are used extensively to produce coatings and thin films for fuel cells, protective coatings, or microelectronic devices. The different techniques used to apply solutions to the substrates can be divided into spraying and sol–gel methods.

Spray deposition methods involve the generation of a fine aerosol from a liquid precursor solution which is then directed towards a heated substrate. Depending on the substrate temperature and precursor used, the droplets evaporate before reaching the substrate or are deposited without evaporation. The atomization of the liquid precursor can be accomplished ultrasonically, by means of a pressurized gas, or through the application of a high electric field to the solution surface at the spray nozzle [130, 131]. Spray pyrolysis in particular exploits an ultrasonically generated aerosol, decomposed by pyrolysis at the heated substrate [132]. When the synthesis employs flame or combustion spray, collision and sintering of the

particles occur in the flame. The substrate temperature is the most important factor in producing high-quality thin films, because it influences droplet drying, decomposition, grain growth, crystallinity, and preferred orientation during the film deposition process. Some reviews report on thin films for solar cells and oxide semiconductor films for gas sensors, relating their properties to their growth characteristics [133–135]. SnO_2 is one of the most widely used thin-film materials prepared by spray pyrolysis. Films grown on glass substrate are highly oriented owing to crystal growth around initially formed nuclei with preferred orientation. Film thickness, growth rate, grain size, and crystallite orientation are influenced by deposition time, substrate temperature, and solution concentration [133]. Similarly ZnO polycrystalline films have been successfully grown with a hexagonal wurtzite structure and mean crystallite size of 20 nm [136]. Above a critical temperature of 600 K the films are *c*-axis oriented [137]. Scanning electron microscopy images of ZnO thin films show that at low substrate temperatures a nonstoichiometric film with rough aspect is obtained, since the reaction kinetics controls the film growth rate process (Figure 1.12a). Figure 1.12b shows a more homogeneous, dense, and crack-free surface. At higher temperatures, a greater rate of vaporization of the solvent occurs away from the substrate and the precursor condenses as microcrystallites in the form of small grains (Figure 1.12c) [138].

In the case of TiO_2 films, phase formation is influenced also by the concentration of precursor solution. At low temperature an increase in precursor concentration modifies the films from amorphous to crystalline anatase. At higher substrate temperature, the oxide changes from a transparent, smooth nanocrystalline anatase film with fine crystalline size (about 10 nm) to opaque crystal aggregates with a larger grain size (50–60 nm) at higher precursor concentration [130]. The use of different solutions can produce porous films where both rutile and anatase phases are present [133].

The sol–gel process is one of the most used liquid-precursor-based techniques in the preparation of thin oxide films. This process is based on liquid-phase hydrolysis of organometallic salts to form a colloidal sol and a condensation step with organic monomers to form a gel. The particle concentration, viscosity, and stability of the sol–gel influence the deposition parameters and film quality. The deposition of films in the sol–gel process proceeds usually through application of a precursor solution on one side of a rapidly rotating substrate (spin coating) or by immersion in the precursor solution (dip coating). A final heating step removes the remaining solvent from the surface. Numerous reviews concerning the sol–gel method (and liquid-based techniques in general) have been published [23, 139]. There have been reports on sol–gel-deposited ZnO films, as well as other materials, where the solution chemistry, the heat treatment conditions, and the substrate type were reported to affect the crystallization behavior and preferred orientation of ZnO films. By varying the density of the coating, it is possible to determine the conditions to yield continuous films characterized by mono-oriented grains with the main axis parallel or perpendicular to the substrate surface and tunable optical response [140, 141]. The degree of orientation

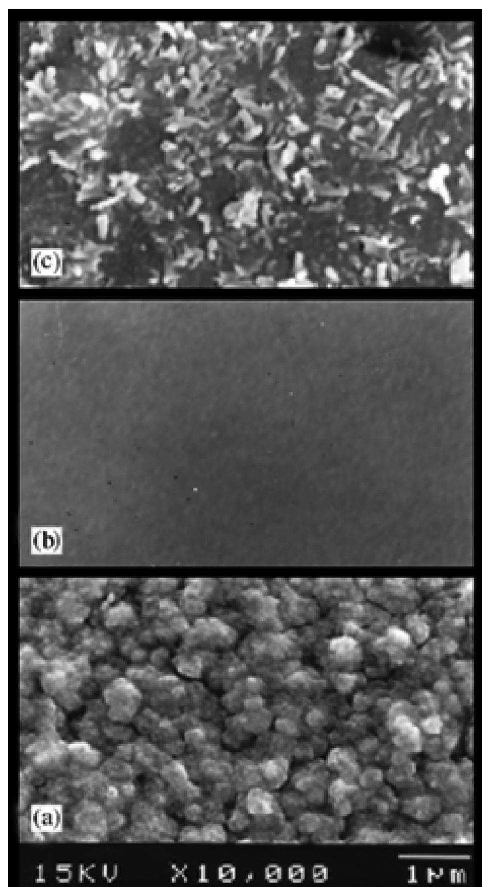

Figure 1.12 Scanning electron microscopy images of ZnO thin film prepared by spray pyrolysis at different temperatures: (a) 473 K; (b) 553 K; (c) 593 K. Reprinted with permission from [138]. Copyright © 2003 Elsevier.

in the films increases with temperature when amorphous substrates are used. In the case of crystalline substrates, no such high degree of orientation was observed, in close relation to the interfacial energy of film and substrate and to the structure of the glass [142]. A variation is reported to produce two-dimensional sub-nanometer oxide films [143]. A gel film is formed on a water surface and deposited layer-by-layer on a substrate by repeated chemisorption and successive hydrolysis. A subsequent heating removes the organics. In this way a uniform TiO_2 film a few angstroms thick is produced after each cycle. Estimation by X-ray photoelectron spectroscopy shows a composition containing carbon and in general the film has the same characteristics as a TiO_2-based gel [144].

1.5
Oxide Nanosheets and Buried Layers

1.5.1
Exfoliated and Detachable Layers

1.5.1.1 Exfoliated Oxide Nanosheets

The delamination of layered compounds is attracting an increasing amount of attention, opening up new fields in the science and technology of two-dimensional nanomaterials. The resulting individual layers can be regarded as a new class of nanoscale materials, referred to as "nanosheets" [145–147]. In particular, oxide nanosheets are exceptionally rich in both structural diversity and electronic properties, with potential application in areas ranging from catalysis to electronics [145–150]. Various nanosheets based on transition metal oxides have been synthesized by delaminating the precursor crystals of layered oxides into their elemental layers. The most well-established method of synthesizing oxide nanosheets is the intercalation reaction with bulky guest species such as tetrabutylammonium ions. In this approach, layered transition metal oxides such as $K_{0.45}MnO_2$ and $KCa_2Nb_3O_{10}$ can be used as the starting material. A common feature of these host compounds is cation-exchange properties involving interlayer alkali metal ions, which are a key to facilitating exfoliation [148]. As the first step to delamination, these layered materials are acid-exchanged into protonated forms such as $H_{0.13}MnO_2 \cdot 0.7H_2O$ and $HCa_2Nb_3O_{10} \cdot 1.5H_2O$, in which the interlayer alkali metal ions can be completely removed under suitable conditions while maintaining the layered structure. The resulting protonic oxides are subsequently delaminated through reaction with a solution containing tetrabutylammonium ions, producing colloidal suspensions of $Ti_{0.91}O_2$, MnO_2, and $Ca_2Nb_3O_{10}$ nanosheets. Such an exfoliation process is quite general: exfoliation of other layered host compounds proceeds in a similar fashion [150]. These materials have prompted many efforts to elucidate their structural properties [145, 148, 149]. The formation of unilamellar nanosheets was confirmed by direct observation with atomic force microscopy (Figure 1.13) and transmission electron microscopy. The average thicknesses ($\pm$ standard deviation) were 0.93 ± 0.06 nm for $Ti_{0.91}O_2$, 0.74 ± 0.10 nm for MnO_2, and 1.84 ± 0.10 nm for $Ca_2Nb_3O_{10}$. The values obtained are nearly comparable to the crystallographic thickness of the host layer in the corresponding parent compounds.

1.5.1.2 Detachable Ultrathin Oxide Films

Anodic oxidation of metal substrates in appropriate electrolyte solutions is an easy, fast, and energy-efficient technique for growing metal oxide films with well-defined thickness and porosity [151, 152]. However, these films are adherent to the substrate surface and are not easily separable, limiting their potential applications. More recently, detachable, porous, and uniform Nb_2O_5, TiO_2, WO_3, and Ta_2O_5 ultrathin films were grown on electropolished niobium, titanium, tungsten, and

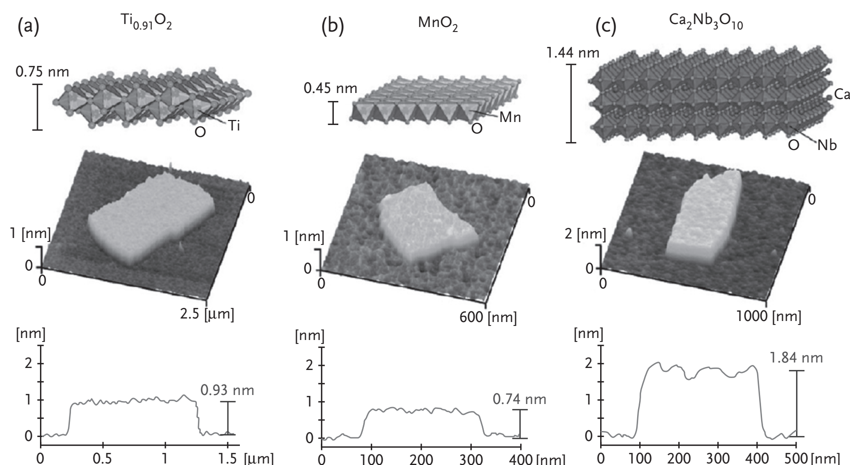

Figure 1.13 Representative structures and atomic force microscopy (AFM) images of selected oxide nanosheets: (a) $Ti_{1-\delta}O_2$ (δ = Ti deficiencies); (b) MnO_2; (c) $Ca_2Nb_3O_{10}$. A tapping-mode AFM instrument with vacuum conditions was used to evaluate the morphology of the nanosheets on Si substrates. Height profiles are also shown. Reprinted with permission from [147]. Copyright © 2009 Royal Society of Chemistry.

tantalum substrate surfaces by anodic oxidation in aqueous electrolytes containing either NH_4F or a mixture of HF and H_2SO_4 [153]. In addition to having catalytic activity, Nb_2O_5, TiO_2, Ta_2O_5, and WO_3 have desirable properties such as high melting points, high refractive indices, piezoelectricity, hardness, high dielectric constants, and excellent chemical stability, which make these films relevant to applications in catalysis, optics, waveguides, electronics, supercapacitors, sensing, and so on. Metal oxide films are formed during anodic oxidation due to the migration of ionic species (F^-, $O_2{}^-$, OH^-) from the electrolyte toward the metal–metal oxide interface and M^{n+} from the metal toward the oxide–electrolyte interface under an applied potential. A thin layer rich in metal oxyfluoride forms *in situ* at the metal–metal oxide interface during anodization due to the higher mobility of F^- compared to $O_2{}^-$. This oxyfluoride layer provides the sacrificial layer for the detachment of the metal oxide layers from the underlying base metal surface. The thickness of each metal oxide membrane sample can be controlled by adjusting the applied voltage and time of anodization (in the range 30–150 nm under current preparative conditions).

1.5.2
Buried Oxide Layers

Point defects in silicon induced by ion implantation have been investigated with regard to doping in silicon device processing [154]. The forward momentum transfer from the implanted ions to the silicon atoms results in the presence of two distinct layers of vacancy excess close to the surface and interstitial excess at

greater depth. These implantation-induced excess defects may serve as nucleation sites for SiO_2 precipitation [155]. This mechanism has been employed for ion beam synthesis of a buried oxide layer in silicon. Most of the oxide precipitates are distributed around the mean projected ion range where the oxygen concentration reaches its maximum. However, many large SiO_2 precipitates are also formed at a shallower depth position around the damage maximum. In order to create a homogeneous continuous buried oxide layer, shrinking of the layer thickness, achieved by the accumulation of the implanted oxygen in only one narrow layer, is essential [155]. Also implanted helium is known to be trapped mainly by vacancy defects to form a helium-filled bubble layer at the position of the vacancy-dominated layer. Such a layer is efficient for gettering of implanted oxygen into a narrow layer [156]. Oxygen gettering at the damage induced by the implantation of a very low implanted oxygen fluence of $10^{17}\ cm^{-2}$ at 185 keV in Si(100) wafers was found to be enhanced by using subsequent helium implantation and employing additional oxygen indiffusion from an annealing atmosphere. In this way, an extremely thin continuous buried oxide layer can be formed [157].

1.6 Conclusions and Perspectives

A number of issues have been raised concerning the growth of ultrathin oxide films, such as the active role of the substrate, the interplay between kinetic and thermodynamic factors, and the importance of the oxidizing agent. The most relevant approaches to film fabrication have also been summarized. The large number of available studies testifies to the increasing importance of this field of research, which expands into the emerging areas of mixed and complex oxides, and of heterostructures coupling oxides with, for example, semiconductors such as silicon and GaAs.

Relevant future trends can be envisaged along various directions:

- the ability to engineer to some extent the surface structure of thin and ultrathin oxide layers via, for example, the epitaxial strain associated with the mismatch between oxide film and substrate, the addition of buffer layer(s), and the control of the film defectivity;
- the ability to tune the size and spatial order of nanoparticles in ordered arrays of self-assembled metal clusters by an appropriate choice of oxide template and of its thickness;
- the ability to control relevant magnetic ordering temperatures and to improve thermal stability in oxide-based magnetic systems, by compensating the finite size effects via coupling with suitable substrates or by exploiting the exchange bias effect, for example, in ferromagnetic (core)–antiferromagnetic (shell) nanoparticles; and
- the development of fabrication methods able to couple scalability (e.g., large numbers, large areas, high rates, poor vacuum, low temperatures) and accurate control of critical film properties.

c01 14 September 2011; 8:43:52

References

1. Freund, H.-J., Kuhlenbeck, H., and Staemmler, V. (1996) *Rep. Prog. Phys.*, **59**, 283–347.
2. Chambers, S.A. (2000) *Surf. Sci. Rep.*, **39**, 105–180.
3. Parkin, S.S.P., Kaiser, C., Panchula, A., Rice, P.M., Hughes, B., Samant, M., and Yang, S.-H. (2004) *Nat. Mater.*, **3**, 862–867.
4. Chambers, S.A., Droubay, T.C., Wang, C.M., Rosso, K.M., Heald, S.M., Schwartz, D.A., Kittilstveld, K.R., and Gamelin, D.R. (2006) *Mater. Today*, **9**, 28–35.
5. Finazzi, M., Duò, L., and Ciccacci, F. (2007) *Surf. Sci. Rep.*, **62**, 337–371.
6. Noguera, C. and Goniakowski, J. (2008) *J. Phys.: Condens. Matter*, **20**, 264003.
7. Freund, H.-J. and Pacchioni, G. (2008) *Chem. Soc. Rev.*, **37**, 2224–2242.
8. Wu, O.-H., Fortunelli, A., and Granozzi, G. (2009) *Int. Rev. Phys. Chem.*, **28**, 517–576.
9. Diebold, U., Li, S.-C., and Schmid, M. (2010) *Ann. Rev. Phys. Chem.*, **61**, 129–148.
10. Duò, L., Finazzi, M., and Ciccacci, F. (2010) *Magnetic Properties of Antiferromagnetic Oxide Materials: Surfaces, Interfaces and Thin Films*, EDS, Wiley-VCH Verlag GmbH, Weinheim.
11. Netzer, F.P., Allegretti, F., and Surnev, S. (2010) *J. Vac. Sci. Technol. B*, **28**, 1–16.
12. Ishikawa, K., Nomura, T., Okada, N., and Takada, K. (1996) *Jpn. J. Appl. Phys.*, **35**, 5196–5198.
13. Tybell, T., Ahn, C.H., and Triscone, J.-M. (1999) *Appl. Phys. Lett.*, **75**, 856–858.
14. Hoffmann, H. (2009) *Angew. Chem. Int. Ed.*, **48**, 2457–2459.
15. Rota, A., Altieri, S., and Valeri, S. (2009) *Phys. Rev. B.*, **79**, 161401(R).
16. Li, F., Parteder, G., Allegretti, F., Franchini, C., Podloucky, R., Surnev, S., and Netzer, F.P. (2009) *J. Phys.: Condens. Matter*, **21**, 134008.
17. Grinter, D.C., Ithnin, R., Pang, C.L., and Thornton, G. (2010) *J. Phys. Chem. C.*, **114**, 17036–17041.
18. Valeri, S., Altieri, S., di Bona, A., Giovanardi, C., and Moia, T.S. (2001) *Thin Solid Films*, **400**, 16–21.
19. Hsieh, S., Liu, G.F., and Koel, B.E. (2008) *J. Vac. Sci. Technol. A.*, **26**, 1336–1342.
20. Busch, M., Gruyters, M., and Winter, H. (2006) *Surf. Sci.*, **600**, 2778–2784.
21. Waddill, G.D. and Ozturk, O. (2005) *Surf. Sci.*, **575**, 35–50.
22. Agnoli, S., Sambi, M., Granozzi, G., Castellarin-Cudia, C., Surnev, S., Ramsey, M.G., and Netzer, F.P. (2004) *Surf. Sci.*, **562**, 150–156.
23. Niesen, T.P. and de Guire, M.R. (2001) *J. Electroceram.*, **6**, 169–207.
24. Choy, K.L. (2003) *Prog. Mater. Sci.*, **48**, 57–170.
25. Franchini, C., Podloucky, R., Allegretti, F., Li, F., Parteder, G., Surnev, S., and Netzer, F.P. (2009) *Phys. Rev. B*, **79**, 035420.
26. Ahn, C.H., Rabe, K.M., and Triscone, J.-M. (2004) *Science*, **303**, 488–491.
27. Csiszar, S.I., Haverkort, M.W., Hu, Z., Tanaka, A., Hsieh, H.H., Lin, H.-J., Chen, C.T., Hibma, T., and Tjeng, L.H. (2005) *Phys. Rev. Lett.*, **95**, 187205.
28. Altieri, S., Finazzi, M., Hsieh, H.H., Lin, H.J., Chen, C.T., Hibma, T., Valeri, S., and Sawatzky, G.A. (2003) *Phys. Rev. Lett.*, **91**, 137201.
29. Dimitrov, D.V., Hadjipanayis, G.C., Papaefthymiou, V., and Simopoulos, A. (1997) *J. Vac. Sci. Technol. A*, **15**, 1473–1477.
30. Goniakowski, J., Finocchi, F., and Noguera, C. (2008) *Rep. Prog. Phys.*, **71**, 016501.
31. Rodriguez, J.A. and Stacchiola, D. (2010) *Phys. Chem. Chem. Phys.*, **12**, 9557–9565.
32. Torelli, P., Soares, E.A., Renaud, G., Gragnaniello, L., Valeri, S., Guo, X.X., and Luches, P. (2008) *Phys. Rev. B*, **77**, 081409(R).
33. Torelli, P., Soares, E.A., Renaud, G., Valeri, S., Guo, X.X., and Luches, P. (2007) *Surf. Sci.*, **601**, 2651–2655.
34. Meyerheim, H.L., Popescu, R., Jedrecy, N., Vedpathak, M., Sauvage-Simkin, M.,

Pinchaux, R., Heinrich, B., and Kirschner, J. (2002) *Phys. Rev. B*, **65**, 144433.
35 Wang, H.-Q., Altman, E.I., and Henrich, V.E. (2008) *Phys. Rev. B*, **77**, 085313.
36 Pierce, J.P., Bartelt, N.C., Stumpf, R., and McCarty, K.F. (2008) *Phys. Rev. B*, **77**, 195438.
37 Agnoli, S., Menteş, T.O., Niño, M.A., Locatelli, A., and Granozzi, G. (2009) *Phys. Chem. Chem. Phys.*, **11**, 3727–3732.
38 Warusawithana, M.P., Cen, C., Sleasman, C.R., Woicik, J.C., Li, Y., Kourkoutis, L.F., Klug, J.A., Li, H., Ryan, P., Wang, L.-P., Bedzyk, M., Muller, D.A., Chen, L.-Q., Levy, J., and Schlom, D.G. (2009) *Science*, **324**, 367–370.
39 Shaikhutdinov, Sh.K. and Weiss, W. (1999) *Surf. Sci.*, **432**, L627–L634.
40 Giovanardi, C., di Bona, A., and Valeri, S. (2004) *Phys. Rev. B*, **69**, 75418.
41 Lu, J., Sundqvist, J., Ottosson, M., Tarre, A., Rosental, A., Aarik, J., and Hårsta, A. (2004) *J. Cryst. Growth*, **260**, 191–200.
42 Zhou, J., Baddorf, A.P., Mullins, D.R., and Overbury, S.H. (2008) *J. Phys. Chem. C*, **112**, 9336–9345.
43 Sutara, F., Cabala, M., Sedlacek, L., Skala, T., Skoda, M., Matolin, V., Prince, K.C., and Chab, V. (2008) *Thin Solid Films*, **516**, 6120–6124.
44 Staudt, T., Lykhach, Y., Hammer, L., Schneider, M.A., Matolín, V., and Libuda, J. (2009) *Surf. Sci.*, **603**, 3382–3388.
45 de Jesus, J.C., Pereira, P., Carrazza, J., and Zaera, F. (1996) *Surf. Sci.*, **369**, 217–230.
46 Goonewardene, A.U., Karunamuni, J., Kurtz, R.L., and Stockbauer, R.L. (2002) *Surf. Sci.*, **501**, 102–111.
47 Bäumer, M., Cappus, D., Kuhlenbeck, H., Freund, H.-J., Wilhelmi, G., Brodde, A., and Neddermeyer, H. (1991) *Surf. Sci.*, **253**, 116–128 and references therein.
48 Muller, F., Steiner, P., Straub, Th., Reinicke, D., Palm, S., de Masi, R., and Hufner, S. (1999) *Surf. Sci.*, **442**, 485–497.
49 Klingenberg, B., Grellner, F., Borgmann, D., and Wedler, G. (1997) *Surf. Sci.*, **383**, 13–24.
50 Mori, K., Yamazaki, M., Hiraki, T., Matsuyama, H., and Koike, K. (2005) *Phys. Rev. B*, **72**, 014418.
51 Takakuwa, Y., Ishidzuka, S., Yoshigoe, A., Teraoka, Y., Yamauchi, Y., Mizuno, Y., Tonda, H., and Homma, T. (2003) *Appl. Surf. Sci.*, **216**, 395–401.
52 Vaquila, I., Passeggi, M.C.G. Jr, and Ferron, J. (1996) *Appl. Surf. Sci.*, **93**, 247–253.
53 Jeurgens, L.P.H., Sloof, W.G., Tichelaar, F.D., and Mittemeijer, E.J. (2002) *Surf. Sci.*, **506**, 313–332.
54 Hasnaoui, A., Politano, O., Salazar, J.M., Aral, G., Kalia, P.K., Nakano, A., and Vashishta, P., *Surf. Sci.*, **579**, 47–57.
55 Starodub, D., Gustafsson, T., and Garfunkel, E. (1994) *Surf. Sci.*, **552**, 199–214.
56 Simon, G.H., König, T., Nilius, M., Rust, H.-P., Heyde, M., and Freund, H.-J. (2008) *Phys. Rev. B*, **78**, 113401.
57 Nishimura, T., Hoshino, Y., Okazawa, T., and Kido, Y. (2008) *Phys. Rev. B*, **77**, 073405.
58 Kelly, P.J. and Arnell, R.D. (2000) *Vacuum*, **56**, 159–172.
59 Uribe, J.D., Osorio, J., Barrero, C.A., Girata, D., Morales, A.L., Devia, A., Gomez, M.E., Ramirez, J.G., and Gancedo, J.R. (2006) *Hyperfine Interact.*, **169**, 1355–1362.
60 Lin, A., Hong, X., Wood, V., Verevkin, A.A., Ahn, C.H., McKee, R.A., Walker, F.J., and Specht, E.D. (2001) *Appl. Phys. Lett.*, **78**, 2034–2036.
61 Aziz, M.J. (2008) *Appl. Phys. A*, **93**, 579–587 and references therein.
62 Ashfold, M.N.R., Claeyssens, F., Fuge, G.M., and Henley, S.J. (2004) *Chem. Soc. Rev.*, **33**, 23–31.
63 Dekkers, M., Nguyen, M.D., Steenwelle, R., Riele, P.M., Blank, D.H.A., and Rijnders, G. (2009) *Appl. Phys. Lett.*, **95**, 012902.
64 Mannhart, J. and Schlom, D.G. (2010) *Science*, **327**, 1607–1611.

65 Dawber, M., Lichtensteiger, C., Cantoni, M., Veithen, M., Ghosez, P., Johnston, K., Rabe, K.M., and Triscone, J.-M. (2005) *Phys. Rev. Lett.*, **95**, 177601.

66 Tsukazaki, A., Ohtomo, A., Kita, T., Ohno, Y., Ohno, H., and Kawasaki, M. (2007) *Science*, **315**, 1388–1391.

67 Mullins, D.R., Overbury, S.H., and Huntley, D.R. (1998) *Surf. Sci.*, **409**, 307–319.

68 Wang, C.H., Jackson, T.J., Somekh, R.E., Leake, J.A., and Evetts, J.E. (1997) *Vacuum*, **48**, 887–889.

69 Phark, S.H., Chang, Y.J., Noh, T.W., and Kim, J.-S. (2009) *Phys. Rev. B*, **80**, 035426.

70 Tanaka, M., Mukai, M., Fujimori, Y., Kondoh, M., Tasaka, Y., Baba, H., and Usami, S. (1996) *Thin Solid Films*, **281–282**, 453–456.

71 Preisler, E.J., Marsh, O.J., Beach, R.A., and McGill, T.C. (2001) *J. Vac. Sci. Technol. B*, **19**, 1611–1618.

72 Hotovy, I., Bùc, D., Hascik, S., and Nennewitz, O. (1998) *Vacuum*, **50**, 41–44.

73 Inoue, T., Ohtake, H., Otani, J., and Shida, S. (2007) *J. Vac. Sci. Technol. A*, **24**, 1128–1132.

74 Šetkus, A., Bukauskas, V., Mironas, A., Senulienė, D., and Strazdienė, V. (2009) *Phys. Stat. Sol. (c)*, **6**, 2753–2755.

75 Ohtomo, A., Muller, D.A., Grazul, J.L., and Hwang, H.Y. (2002) *Nature*, **419**, 378–380.

76 Vailionis, A., Boschker, H., Houwman, E., Koster, G., Rijnders, G., and Blank, D.H.A. (2009) *Appl. Phys. Lett.*, **95**, 152508.

77 Wollschläger, J., Viernow, J., Tegenkamp, C., Erdös, D., Schröder, K.M., and Pfnür, H. (1999) *Appl. Surf. Sci.*, **142**, 129–134.

78 Schintke, S., Messerli, S., Pivetta, M., Patthey, F., Libioulle, L., Stengel, M., De Vita, A., and Schneider, W.D (2001) *Phys. Rev. Lett.*, **87**, 276801.

79 Valeri, S., Altieri, S., di Bona, A., Luches, P., Giovanardi, C., and Moia, T.S. (2002) *Surf. Sci.*, **507–510**, 311–317.

80 Valeri, S., Altieri, S., del Pennino, U., di Bona, A., Luches, P., and Rota., A. (2002) *Phys. Rev. B*, **65**, 245410.

81 Meyerheim, H.L., Popescu, R., Kirschner, J., Jedrecy, N., Sauvage-Simkin, M., Heinrich, B., and Pinchaux, R. (2001) *Phys. Rev. Lett.*, **87**, 076102.

82 Klaua, M., Ullmann, D., Barthel, J., Wulfhekel, W., Kirschner, J., Urban, R., Monchesky, T.L., Enders, A., Cochran, J.F., and Heinrich, B. (2001) *Phys. Rev. B*, **64**, 134411.

83 Gallagher, M.C., Fyfield, M.S., Bumm, L.A., Cowin, J.P., and Joyce, S.A. (2003) *Thin Solid Films*, **445**, 90–95.

84 Sterrer, M., Fischbach, E., Risse, T., and Freund, H.-J. (2005) *Phys. Rev. Lett.*, **94**, 186101.

85 Benedetti, S., Benia, H.M., Nilius, N., Valeri, S., and Freund, H.J. (2006) *Chem. Phys. Lett.*, **430**, 330–335.

86 Benedetti, S., Torelli, P., Valeri, S., Benia, H.M., Nilius, N., and Renaud, G. (2008) *Phys. Rev. B*, **78**, 195411.

87 Wollschläger, J., Erdös, D., Goldbach, H., Höpken, R., and Schröder, K.M. (2001) *Thin Solid Films*, **400**, 1–8.

88 Kramer, J., Ernst, W., Tegenkamp, C., and Pfnür, H. (2002) *Surf. Sci.*, **517**, 87–97.

89 Ferrari, A.M., Casassa, S., Pisani, C., Altieri, S., Rota, A., and Valeri, S. (2005) *Surf. Sci.*, **588**, 160–166.

90 Valeri, S., Luches, P., and Altieri, S. (2010) in *Magnetic Properties of Antiferromagnetic Oxide Materials: Surfaces, Interfaces and Thin Films* (eds Duò, L., Finazzi, M., and Ciccacci, F.), Wiley-VCH Verlag GmbH, Weinheim, pp. 25–68.

91 Schoiswohl, J., Zheng, W., Surnev, S., Ramsey, M.G., Granozzi, G., Agnoli, S., and Netzer, F.P. (2006) *Surf. Sci.*, **600**, 1099–1106.

92 Biedermann, K., Gubo, M., Hammer, L., and Heinz, K. (2009) *J. Phys.: Condens. Matter*, **21**, 185003.

93 Giordano, L., Pacchioni, G., and Goniakowski, J. (2007) *Phys. Rev. B*, **76**, 075416.

94 Maheswaran, S., Thevuthasan, S., Gao, F., Shutthanandan, V., Wang, C.M.,

and Smith, R.J. (2005) *Phys. Rev. B*, **72**, 075403.

95 Surnev, L., Kresse, G., Ramsey, J.A., and Netzer, F.P. (2001) *Phys. Rev. Lett.*, **87**, 86102.

96 Surnev, S., Sock, M., Kresse, G., Andersen, J.N., Ramsey, M.G., and Netzer, F.P. (2003) *J. Phys. Chem. B*, **107**, 4777–4785.

97 Schoiswohl, J., Sock, M., Surnev, S., Ramsey, M.G., Netzer, F.P., Kresse, G., and Andersen, J.N. (2004) *Surf. Sci.*, **555**, 101–117.

98 Simic-Milosevic, V., Nilius, N., Rust, H.P., and Freund, H.-J. (2008) *Phys. Rev. B*, **77**, 125112.

99 Abu Haija, M., Guimond, S., Romanyshyn, Y., Uhl, A., Kuhlenbeck, H., Todorova, T.K., Ganduglia-Pirovano, M.V., Dobler, J., Sauer, J., and Freund, H.J. (2006) *Surf. Sci.*, **600**, 1497–1503.

100 Sedona, F., Agnoli, S., and Granozzi, G. (2006) *J. Phys. Chem. B*, **110**, 15359–15367.

101 Sedona, F., Agnoli, S., Fanetti, M., Kholmanov, I., Cavaliere, E., Gavioli, L., and Granozzi, G. (2007) *J. Phys. Chem. C*, **111**, 8024–8029.

102 Sedona, F., Rizzi, G.A., Agnoli, S., Llabres i Xamena, F.X., Papageorgiou, A., Osterman, D., Sambi, M., Finetti, P., Schierbaum, K., and Granozzi, G. (2005) *J. Phys. Chem. B*, **109**, 24411–24426.

103 Barcaro, G., Agnoli, S., Sedona, F., Rizzi, G.A., Fortunelli, A., and Granozzi, G. (2009) *J. Phys. Chem. C*, **113**, 5721–5729.

104 Logvenov, G., Gozar, A., and Bozovic, I. (2009) *Science*, **326**, 699–702.

105 Schroeder, T., Adelt, M., Richter, B., Naschitzki, M., Giorgi, J.B., Bäumer, M., and Freund, H.-J. (2000) *Surf. Rev. Lett.*, **7**, 7–14.

106 Weissenrieder, J., Kaya, S., Lu, J.-L., Gao, H.-J., Shaikhutdinov, S., Freund, H.-J., Sierka, M., Todorova, T.K., and Sauer, J. (2005) *Phys. Rev. Lett.*, **95**, 076103.

107 Vurens, G.H., Maurice, V., Salmeron, M., and Somorjai, G.A. (1992) *Surf. Sci.*, **268**, 170–178.

108 Sambi, M., Sensolo, R., Rizzi, G.A., Petukhov, M., and Granozzi, G. (2003) *Surf. Sci.*, **537**, 36–54.

109 Schoiswohl, J., Sock, M., Eck, S., Surnev, S., Ramsey, M.G., Netzer, F.P., and Kresse, G. (2004) *Phys. Rev. B*, **69**, 155403.

110 Entani, S., Kiguchi, M., and Koichiro, S. (2004) *Surf. Sci.*, **566–568**, 165–169.

111 Matsumoto, T., Batzill, M., Hsieh, S., and Koel, B.E. (2004) *Surf. Sci.*, **572**, 127–145.

112 Knight, P.J., Toomes, R., Driver, S.M., and Woodruff, D.P. (1998) *Surf. Sci.*, **418**, 521–528.

113 Chang, P.C., Fan, Z., Wang, D., Tseng, W.Y., Chiou, W.A., Hong, J., and Lu, J.G. (2004) *Chem. Mater.*, **16**, 5133–5137.

114 Tominaga, K., Sakashita, Y., Nakashima, H., and Okada, M. (1994) *J. Cryst. Growth*, **145**, 219–225.

115 Endo, K., Yamasaki, H., Misawa, S., Yoshida, S., and Kajimura, K. (1992) *Nature*, **355**, 327–328.

116 Kumar, N.D., Kamalasanan, M.N., and Chandra, S. (1994) *Appl. Phys. Lett.*, **65**, 1373–1375.

117 Carta, G., El Habra, N., Crociani, L., Rossetto, G., Zanella, P., Zanella, A., Paolucci, G., Barreca, D., and Tondello, E. (2007) *Chem. Vap. Deposition*, **13**, 185–189.

118 Boo, J.-H., Lee, S.-B., Yu, K.-S., Koh, W., and Kim, Y. (1999) *Thin Solid Films*, **341**, 63–67.

119 Niinisto, L., Ritala, M., and Leskela, M. (1996) *Mater. Sci. Eng. B*, **41**, 23–29.

120 George, S.M., Ott, A.W., and Klaus, J.W. (1996) *J. Phys. Chem.*, **100**, 13121–13131.

121 Niinistö, L., Päiväsaari, J., Niinistö, J., Putkonen, M., and Nieminen, M. (2004) *Phys. Stat. Sol. (a)*, **201**, 1443–1452.

122 Leskel, M. and Ritala, M. (2003) *Angew. Chem. Int. Ed.*, **42**, 5548–5554.

123 Cassir, M., Ringuedé, A., and Niinisto, L. (2010) *J. Mater. Chem.*, **20**, 8987–8993.

124 Du, X., Du, Y., and George, S.M. (2008) *J. Phys. Chem. A*, **112**, 9211–9219.

125 Elam, J.W. and George, S.M. (2003) *Chem. Mater.*, **15**, 1020–1028.

126 Ritala, M., Leskela, M., Niinisto, L., and Haussalo, P. (1993) *Chem. Mater.*, **5**, 1174–1181.

127 Burton, B.B., Goldstein, D.N., and George, S.M. (2009) *J. Phys. Chem. C*, **113**, 1939–1946.

128 Jones, A.C., Aspinall, H.C., Chalker, P.R., Potter, R.J., Manning, T.D., Loo, Y.F., O'Kane, R., Gaskell, J.M., and Smith, L.M. (2006) *Chem. Vap. Deposition*, **12**, 83–98.

129 Sundqvist, J., Lu, J., Ottosson, M., and Hårsta, A. (2006) *Thin Solid Films*, **514**, 63–68.

130 Choy, K. (2001) *Mater. Sci. Eng. C*, **16**, 139–145.

131 Chen, C.H., Emond, M.H.J., Kelder, E.M., Meester, B., and Schoonman, J. (1999) *J. Aerosol Sci.*, **30**, 959–967.

132 Choy, K.L. (2000) in *Handbook of Nanostructured Materials and Nanotechnology*. (ed Nalwa, H.S.), Academic Press, San Diego, p. 533.

133 Patil, P.S. (1999) *Mater. Chem. Phys.*, **59**, 185–198.

134 Studenikin, S.A., Golego, N., and Cocivera, M. (1998) *J. Appl. Phys.*, **84**, 2287–2294.

135 Korotcenkov, G. (2005) *Sens. Actuators B*, **107**, 209–232.

136 Yoshino, K., Fukushima, T., and Yoneta, M. (2005) *J. Mater. Sci. Mater. Electr.*, **16**, 403–408.

137 Paraguay, F., Estrada, W., Acosta, D.R., Andrade, E., and Miki-Yoshida, M. (1999) *Thin Solid Films*, **350**, 192–202.

138 Ayouchi, R., Martin, F., Leinen, D., and Ramos-Barrado, J.R. (2003) *J. Cryst. Growth*, **247**, 497–504.

139 Bhuiyan, M.S., Paranthaman, M., and Salama, K. (2006) *Supercond. Sci. Technol.*, **19**, R1–R21.

140 Znaidi, L. (2010) *Mater. Sci. Eng. B*, **174**, 18–30.

141 Znaidi, L., Illia, G.J.A.A.S., Benyahia, S., Sanchez, C., and Kanaev, A.V. (2003) *Thin Solid Films*, **428**, 257–262.

142 Chakrabarti, S., Ganguli, D., and Chaudhuri, S. (2004) *Mater. Lett.*, **58**, 3952–3957.

143 Moriguchi, I., Maeda, H., Teraoka, Y., and Kagawa, S. (1995) *J. Am. Chem. Soc.*, **117**, 1139–1140.

144 Ichinose, I., Senzu, H., and Kunitake, T. (1997) *Chem. Mater.*, **9**, 1296–1298.

145 Sasaki, T. and Watanabe, M. (1998) *J. Am. Chem. Soc.*, **120**, 4682–4689.

146 Sasaki, T. (2007) *J. Ceram. Soc. Jpn.*, **115**, 9–16.

147 Osada, M. and Sasaki, T. (2009) *J. Mater. Chem.*, **19**, 2503–2511.

148 Omomo, Y., Sasaki, T., Wang, L.Z., and Watanabe, M. (2003) *J. Am. Chem. Soc.*, **125**, 3568–3575.

149 Ebina, Y., Sasaki, T. and Watanabe, M. (2002) *Solid State Ionics*, **151**, 177–182.

150 Ozawa, T.C., Fukuda, K., Akatsuka, K., Ebina, Y., Sasaki, T., Kurashima, K., and Kosuda, K. (2008) *J. Phys. Chem. C*, **112**, 1312–1315.

151 Lee, W., Ji, R., Gösele, U., and Nielsch, K. (2006) *Nat. Mater.*, **5**, 741–747.

152 Schwirn, K., Lee, W., Hillebrand, R., Steinhart, M., Nielsch, K., and Gösele, U. (2008) *ACS Nano*, **2**, 302–310.

153 Singh, S., Festin, M., Barden, W.R.T., Xi, L., Francis, J.T., and Kruse, P. (2008) *ACS Nano*, **2**, 2363–2373.

154 Kyllesbech Larsen, K., Privitera, V., Coffa, S., Priolo, F., Campisano, S.U., and Carnera, A. (1996) *Phys. Rev. Lett.*, **76**, 1493–1496.

155 Kögler, R., Ou, X., Skorupa, W., and Möller, W. (2008) *Appl. Phys. Lett.*, **92**, 181906.

156 Ou, X., Kögler, R., Mücklich, A., Skorupa, W., Möller, W., Wang, X., Gerlach, J.W., and Rauschenbach, B. (2008) *Appl. Phys. Lett.*, **93**, 161907.

157 Ou, X., Kögler, R., Mücklich, A., Skorupa, W., Möller, W., Wang, X., and Vines, L. (2009) *Appl. Phys. Lett.*, **94**, 011903.